Front. Mech. Eng. 2020, 15(1): 43–54
https://doi.org/10.1007/s11465-019-0547-9

RESEARCH ARTICLE

Lijun XIAO, Ming WANG, Bangji ZHANG, Zhihua ZHONG

Vehicle roll stability control with active roll-resistant electro-hydraulic suspension

Abstract This study examines roll stability control for vehicles with an active roll-resistant electro-hydraulic suspension (RREHS) subsystem under steering maneuvers. First, we derive a vehicle model with four degrees of freedom and incorporates yaw and roll motions. Second, an optimal linear quadratic regulator controller is obtained in consideration of dynamic vehicle performance. Third, an RREHS subsystem with an electric servo-valve actuator is proposed, and the corresponding dynamic equations are obtained. Fourth, field experiments are conducted to validate the performance of the vehicle model under sine-wave and double-lane-change steering maneuvers. Finally, the effectiveness of the active RREHS is determined by examining vehicle responses under sine-wave and double-lane-change maneuvers. The enhancement in vehicle roll stability through the RREHS subsystem is also verified.

Keywords electro-hydraulic suspension, roll stability, LQR, experiment

1 Introduction

According to statistics from the US National Highway Traffic Safety Administration, rollover crashes contribute 33% to the total number of fatal deaths in the USA, although they account for only 3% of all passenger car crashes [1]. Vehicle rollover accidents are among the most common fatal causes of human death [2]. Consequently, vehicle roll motion control has become a prevalent research topic [3–6]. Vehicle suspension, which minimizes the vibrations of occupants caused by road disturbances, is the most important system for vehicle roll stability enhancement. Various strategies have been applied to vehicle suspension systems, and these can be generally categorized as passive suspension (optimization of the suspension system) [7–9], semi-active suspension [10–12], and active suspension [13–16]. Enhancing the roll motions of vehicles with active suspension systems is crucial.

Considering the importance of suspension systems in enhancing ride comfort and holding capacity, various suspension systems have been developed over the decades [17–20]. Among them, the electro-hydraulic suspension has received extensive attention from industrial and academic circles. Du and Zhang [21] introduced an electrohydraulic suspension for vehicles with actuator constraints. Choi et al. [22] presented a fuzzy controller for electro-hydraulic suspension systems with preview information on road disturbances. Sun et al. [23] used electro-hydraulic suspension to improve vehicle ride comfort without sacrificing road holding capacity with limitations in vehicle parameter uncertainties. These studies have revealed that electro-hydraulic suspension is mainly used to enhance vehicle ride comfort. However, the application of this type of suspension in vehicle roll motion control has not been investigated.

For decades, researchers have exerted effort to enhance vehicle roll motion by using various control strategies. Kim [24] developed an electrically actuated roll control system to enhance vehicle roll behavior under parameter perturbation. Yim [25] used previewable information on steering input to design a static output feedback linear quadratic regulator (LQR) controller to avoid extreme roll motion situations. Huang et al. [26] developed a state derivative-induced LQR controller to reduce the rollover risk of heavy articulated vehicles. Imine et al. [27] used a twisting-sliding mode scheme to ensure roll stability via an active steering assistant system. Dal Poggetto and Serpa [28] utilized a gain-scheduled LQR controller to reduce the possibility of vehicle rollover. The mechanisms through which vehicle velocity influences the controller gain were also investigated. Sun et al. [29] developed an active stabilizer bar in consideration of fast-varying sprung mass. Pourasad et al. [30] and Marzbanrad et al. [31] improved vehicle path following, roll, and handling performance

Received April 21, 2019; accepted May 24, 2019

Lijun XIAO, Ming WANG (✉), Bangji ZHANG, Zhihua ZHONG
State Key Laboratory of Advanced Design and Manufacture for Vehicle Body, Hunan University, Changsha 410082, China
E-mail: to_wm@hnu.edu.cn

simultaneously by using LQR controllers and fuzzy logic respectively. These studies have improved vehicle roll motion behavior with various control schemes. However, the application of electro-hydraulic suspension to the enhancement of vehicle roll motion still needs to be improved.

The integration of electro-hydraulic suspension and active controller can effectively enhance vehicle performance [32–34]. However, the majority of relevant studies mainly used one servo-valve to actuate one hydraulic suspension, and this usage consumes much energy. In this study, a cross-linked hydraulic suspension uses only one servo-valve to actuate two hydraulic suspensions; thus, less fuel is used. In addition, due to the natural merit of the cross-linked shape, the proposed electro-hydraulic suspension can effectively enhance vehicle roll stability without affecting other aspects, such as bounce and pitch motions. An active roll-resistant electro-hydraulic suspension (RREHS) subsystem controlled by the LQR scheme is also proposed to enhance vehicle performance. The primary contributions of this study are as follows: (1) An active RREHS subsystem is proposed, and (2) a vehicle model with four degrees of freedom (DOFs) and incorporates yaw and roll motions is developed and validated via field experiments.

The rest of the paper is organized as follows. In Section 2, the 4-DOF vehicle model and the LQR controller for generating roll-resistant moments are presented. In Section 3, the RREHS subsystem with an electro-servo valve actuator is introduced. In Section 4, vehicle model validation is conducted via field tests using a fully electric vehicle prototype. The effectiveness of the RREHS subsystem with an optimal control scheme is also investigated under sine-wave and double-lane-change maneuvers. Section 5 presents the main conclusions.

2 Vehicle model and LQR controller

A vehicle model that incorporates yaw and roll motions is formulated. Then, the LQR control scheme utilized to actuate the electro-hydraulic suspension is provided.

First, a 4-DOF vehicle model is utilized to characterize lateral and roll motions. The vehicle is assumed to run on an even road surface to simplify the modeling. Therefore, the wheel motions can be simplified as the average roll angle displacement of unsprung mass ϕ_u, as shown in Fig. 1(b). The vehicle sideslip angle at the center of gravity (CG) β, yaw angle ψ, and roll angle ϕ are the three other DOFs, as shown in Fig. 1. For brevity, the following assumptions are established: (i) roll angles ϕ and ϕ_u are small enough, and (ii) the vehicle's longitudinal velocity v_x is considered to be constant.

From Fig. 1, the dynamic equations on vehicle yaw motion can be derived as follows:

$$\begin{bmatrix} (m_s+2m_{uf}+2m_{ur})v_x & 2(m_{uf}l_f-m_{ur}l_r) \\ 2(m_{uf}l_f-m_{ur}l_r)v_x & I_{zz} \end{bmatrix} \begin{bmatrix} \dot\beta+\dot\psi \\ \ddot\psi \end{bmatrix} = \begin{bmatrix} \sum_{i=1}^{4} F_{yui}+m_s h_{os}\ddot\phi \\ M_{zu} \end{bmatrix}, \quad (1)$$

where m_s is the sprung mass, m_{uf} and m_{ur} are the front and the rear unsprung masses, respectively, l_f and l_r are the lengths from CG to the front and rear axle, respectively, $I_{zz}=I_{szz}+2m_{uf}(l_f^2+t_f^2)+2m_{ur}(l_r^2+t_r^2)$ is the yaw inertia of the vehicle, h_{os} is the height from vehicle rolling center to CG of sprung mass, F_{yui} pertain to the lateral tire forces generated by the Dugoff tire model [35], and $M_{zu}=[l_f,\ l_f,\ -l_r,\ -l_r]\boldsymbol{F}_{yu}$ is the yaw momentum with $\boldsymbol{F}_{yu}=[F_{yu1}, F_{yu2}, F_{yu3}, F_{yu4}]^T$.

The suspension deflections and relative velocities can be obtained in consideration of vehicle geometry. The suspension forces ($\boldsymbol{F}_s$) generated by the original mechanical suspension can be derived as follows:

$$\boldsymbol{F}_s=\boldsymbol{C}_s\boldsymbol{T}(\dot\phi-\dot\phi_u)+\boldsymbol{K}_s\boldsymbol{T}(\phi-\phi_u), \quad (2)$$

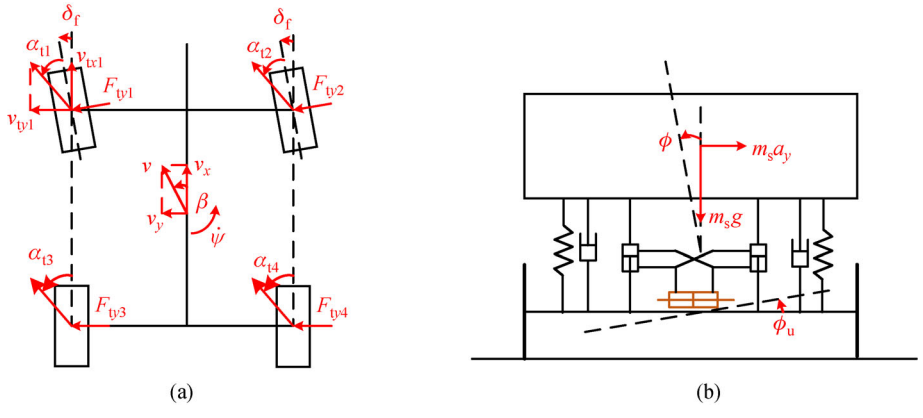

Fig. 1 4-DOF vehicle model. (a) Lateral representation; (b) vertical representation of half-vehicle.

where $\boldsymbol{K}_s$= diag([k_{sf}, k_{sf}, k_{sr}, k_{sr}]), $\boldsymbol{C}_s$= diag([c_{sf}, c_{sf}, c_{sr}, c_{sr}]), k_{sf} and k_{sr} are the stiffnesses of the front and the rear suspension, c_{sf} and c_{sr} are the dampers of the front and the rear suspension, respectively, and $\boldsymbol{T}$=[$-t_f$, t_f, $-t_r$, t_r]^T is the geometry transformation matrix, and t_f and t_r are the half-track widths of the front and the rear axle.

Then, the moment balance of sprung mass along the longitudinal axis can be obtained as

$$I_s\ddot{\phi} + m_s g h_{os}\sin\phi - m_s a_y h_{os}\cos\phi + \boldsymbol{T}^T\boldsymbol{F}_s + u(t) = 0, \tag{3}$$

where I_s is the roll inertia of sprung mass, $a_y = \dot{v}_y + v_x\dot{\psi}$ is the lateral acceleration, and $u(t)$ is the active roll-resistant moment generated by the RREHS.

The force balance of the unsprung masses can also be obtained as

$$\boldsymbol{M}_u\ddot{\boldsymbol{Z}}_u + \boldsymbol{C}_s(\dot{\boldsymbol{Z}}_u - \boldsymbol{T}\dot{\phi}) + \boldsymbol{K}_s(\boldsymbol{Z}_u - \boldsymbol{T}\phi) + \boldsymbol{C}_t(\dot{\boldsymbol{Z}}_u - \dot{\boldsymbol{Z}}_g)$$

$$+\boldsymbol{K}_t(\boldsymbol{Z}_u - \boldsymbol{Z}_g) = \boldsymbol{0}, \tag{4}$$

where $\boldsymbol{M}_u$= diag([m_{uf}, m_{uf}, m_{ur}, m_{ur}]), $\boldsymbol{C}_t$= diag([c_{tf}, c_{tf}, c_{tr}, c_{tr}]), $\boldsymbol{K}_t$= diag([k_{tf}, k_{tf}, k_{tr}, k_{tr}]), c_{tf} and c_{tr} are the dampers of the front and the rear tyre, respectively, k_{tf} and k_{tr} are the vertical stiffnesses of the front and the rear tyre, respectively, $\boldsymbol{Z}_u$= $\boldsymbol{T}\phi_u$ is the vertical displacement of the unsprung masses, and $\boldsymbol{Z}_g$= $\boldsymbol{0}$ is the road input vector for wheels.

Equation (4) can be further rewritten by left-multiplying $\boldsymbol{T}^T$ as follows:

$$I_u\ddot{\phi}_u + c_s(\dot{\phi}_u - \dot{\phi}) + k_s(\phi_u - \phi) + c_t\dot{\phi}_u + k_t\phi_u - u(t) = 0, \tag{5}$$

where $I_u = 2m_{uf}t_f^2 + 2m_{ur}t_r^2$ is the equivalent roll inertia of unsprung mases, $c_s = 2t_f^2c_{sf} + 2t_r^2c_{sr}$, $k_s = 2t_f^2k_{sf} + 2t_r^2k_{sr}$, $c_t = 2t_f^2c_{tf} + 2t_r^2c_{tr}$, and $k_t = 2t_f^2k_{tf} + 2t_r^2k_{tr}$.

By defining $\boldsymbol{x} = \left[\phi - \phi_u,\ \phi_u,\ \dot{\phi},\ \dot{\phi}_u\right]^T$, the state-space model for the subsystem in Eqs. (3) and (5) can be derived as follows:

$$\dot{\boldsymbol{x}}(t) = \boldsymbol{A}\boldsymbol{x}(t) + \boldsymbol{B}_1 w(t) + \boldsymbol{B}u(t), \tag{6}$$

where $w(t)$= $a_y - g\phi$ and

$$\boldsymbol{A} = \begin{bmatrix} 0 & 0 & 1 & -1 \\ 0 & 0 & 0 & 1 \\ -\dfrac{k_s}{I_s} & 0 & -\dfrac{c_s}{I_s} & \dfrac{c_s}{I_s} \\ \dfrac{k_s}{I_u} & -\dfrac{k_t}{I_u} & \dfrac{c_s}{I_u} & -\dfrac{c_s + c_t}{I_u} \end{bmatrix},$$

$$\boldsymbol{B}_1 = \begin{bmatrix} 0 \\ 0 \\ \dfrac{m_s h_{os}}{I_s} \\ 0 \end{bmatrix},\ \boldsymbol{B} = \begin{bmatrix} 0 \\ 0 \\ \dfrac{1}{I_s} \\ -\dfrac{1}{I_u} \end{bmatrix}.$$

The main objective of this work is to design a linear quadratic controller to improve vehicle dynamic performance [36], which generally consists of the following aspects:

(i) **Roll stability**: Vehicle roll stability is generally characterized by the lateral load transfer ratio, which is affected by sprung mass roll angle and lateral acceleration. However, lateral acceleration cannot be minimized when the longitudinal velocity and path curvature are prescribed. We can minimize the roll angle of vehicle sprung mass ϕ to help improve vehicle roll stability.

(ii) **Suspension deflections**: Excessive suspension deflections may deteriorate vehicle ride comfort and even cause structural damage. Considering that only the front axle is equipped with electro-hydraulic suspension, the suspension deflections at the front axle, which are proportional to ($\phi - \phi_u$) in this work, should be minimized to avoid vehicle performance deterioration.

(iii) **Vehicle safety**: A firm uninterrupted tire-terrain contact is a prerequisite for vehicle lateral stability, which is generally characterized by ϕ_u in this work. Therefore, the tire-terrain angle difference should also be minimized.

The maximum value of the actuator output forces should be constrained so that the actuator input voltage is physically limited.

On the basis of these analyses, the quadratic cost function and the hard constraint on actuator force can be formulated as follows:

$$J = \int_0^t \boldsymbol{y}^T\boldsymbol{Q}\boldsymbol{y}\mathrm{d}t + \int_0^t u^T R u\mathrm{d}t, \tag{7}$$

$$|u| \leqslant u_{max}, \quad |\phi - \phi_u| \leqslant \phi_{max}, \tag{8}$$

where $\boldsymbol{Q}$ and R are the known positive-definite matrices with weight coefficients in $\boldsymbol{y}$ and u in their diagonals respectively, u_{max} is the upper bound of control input, ϕ_{max} is the maximum roll angle allowed, and $\boldsymbol{y} = \boldsymbol{C}\boldsymbol{x}$, where

$$\boldsymbol{C} = \begin{bmatrix} 1 & 1 & 0 & 0 \\ 1 & 0 & 0 & 0 \\ 0 & 1 & 0 & 0 \end{bmatrix}.$$

With these analyses, we define the controller gain as $\boldsymbol{K} = -R^{-1}\boldsymbol{B}^T\boldsymbol{P}$, where $\boldsymbol{P}$ satisfies the Riccati function:

$$\boldsymbol{A}^T\boldsymbol{P} + \boldsymbol{P}\boldsymbol{A} - \boldsymbol{P}\boldsymbol{B}R^{-1}\boldsymbol{B}^T\boldsymbol{P} + \boldsymbol{C}^T\boldsymbol{Q}\boldsymbol{C} = \boldsymbol{0}. \tag{9}$$

Then, external force $u(t)=\boldsymbol{K}\boldsymbol{x}(t)$ is derived and generated with the electro-hydraulic actuator through Eq. (11), and the actuator outputs can be obtained with Eqs. (16) and (17). In consideration of vehicle performance, the weight matrices are set as

$$\boldsymbol{Q}=\begin{bmatrix}10^5 & 0 & 0\\ 0 & 10^5 & 0\\ 0 & 0 & 1\end{bmatrix},\quad R=10^{-4}. \tag{10}$$

3 Electro-hydraulic suspension

Figure 2 shows a diagram of the proposed RREHS subsystem, which consists of a servo-valve (or proportional valve) hydraulic actuator, two cylinders, and several oil pipes.

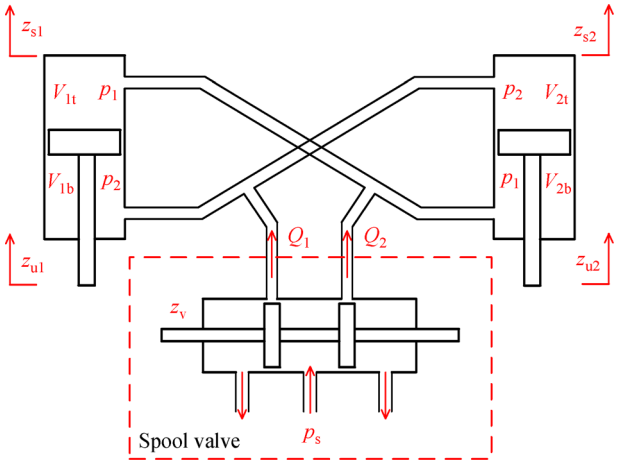

Fig. 2 Schematic of the electrohydraulic actuator.

The spool valve of the electronic servo-valve is controlled by electric current to produce displacement z_v. Oil supply high pressure p_s is generally stored outside the electronic servo-valve, and the moving spool valve distributes high-pressure oil to two oil circuits [37].

The chamber section area differences in the two hydraulic cylinders are assumed to be negligible in this work. Thus, the vertical force generated by the RREHS subsystem acting on the vehicle system is equal to zero, and roll moment $u(t)$ from the RREHS subsystem can be formulated as

$$u(t)=(p_1-p_2)A_ct_h-(p_2-p_1)A_ct_h=2\Delta pA_ct_h. \tag{11}$$

where p_1 and p_2 are the pressures of pipelines, A_c is the piston area, t_h is the length of chambers, and Δp is the pressure difference between top and bottom chambers.

The fluid quantities for each oil circuit can be derived as follows:

$$\begin{cases}\dfrac{\mathrm{d}}{\mathrm{d}t}(V_{1t}+V_{2b})+\dfrac{1}{\beta_e}(V_{1t}+V_{2b})\dfrac{\mathrm{d}p_1}{\mathrm{d}t}\\ \quad=Q_1-C_{ip}(p_1-p_2)-C_{ep}p_1,\\ \dfrac{\mathrm{d}}{\mathrm{d}t}(V_{2t}+V_{1b})+\dfrac{1}{\beta_e}(V_{2t}+V_{1b})\dfrac{\mathrm{d}p_2}{\mathrm{d}t}\\ \quad=Q_2+C_{ip}(p_1-p_2)-C_{ep}p_2,\end{cases} \tag{12}$$

where β_e is the effective bulk modulus of the oil, C_{ep} and C_{ip} are the external and internal leakage coefficients of the cylinders, respectively, Q_1 and Q_2 represent the flow quantities of spool valve, V_{1t} and V_{2t} represent the volume of the top chamber of left and right cylinder, respectively, V_{1b} and V_{2b} represent the volume of bottom chamber of left and right cylinder, respectively.

The volumes in each chamber can be determined with the relative displacements of the cylinders as follows:

$$V_{1t}=V_{10}+A_c(z_{s1}-z_{u1}),\ V_{1b}=V_{20}-A_c(z_{s1}-z_{u1}),$$
$$V_{2t}=V_{10}+A_c(z_{s2}-z_{u2}),\ V_{2b}=V_{20}-A_c(z_{s2}-z_{u2}), \tag{13}$$

where V_{10} and V_{20} are the initial volumes in the top and bottom chambers, respectively, z_{s1} and z_{s2} are the vertical displacements of the cylinders block, and z_{u1} and z_{u2} are the vertical displacements of the piston rod.

With Eqs. (12) and (13), the dynamic equations in the two oil circuits can be formulated as

$$\begin{cases}\dfrac{\mathrm{d}}{\mathrm{d}t}(A_c(z_{s1}-z_{u1})-A_c(z_{s2}-z_{u2}))\\ \quad+\dfrac{1}{\beta_e}(V_{10}+V_{20}+A_c(z_{s1}-z_{u1})-A_c(z_{s2}-z_{u2}))\dfrac{\mathrm{d}p_1}{\mathrm{d}t}\\ \quad=Q_1-C_{ip}(p_1-p_2)-C_{ep}p_1,\\ \dfrac{\mathrm{d}}{\mathrm{d}t}(A_c(z_{s2}-z_{u2})-A_c(z_{s1}-z_{u1}))\\ \quad+\dfrac{1}{\beta_e}(V_{10}+V_{20}+A_c(z_{s2}-z_{u2})-A_c(z_{s1}-z_{u1}))\dfrac{\mathrm{d}p_2}{\mathrm{d}t}\\ \quad=Q_2+C_{ip}(p_1-p_2)-C_{ep}p_2.\end{cases} \tag{14}$$

With Eq. (14), we derive

$$2A_c\frac{\mathrm{d}}{\mathrm{d}t}((z_{s1}-z_{u1})-(z_{s2}-z_{u2}))+\frac{1}{\beta_e}(V_{10}+V_{20})\frac{\mathrm{d}}{\mathrm{d}t}(p_1-p_2)$$
$$+\frac{1}{\beta_e}(A_c(z_{s1}-z_{u1})-A_c(z_{s2}-z_{u2}))\frac{\mathrm{d}}{\mathrm{d}t}(p_1+p_2)$$
$$=Q_1-Q_2-(2C_{ip}+C_{ep})(p_1-p_2). \tag{15}$$

Considering that $p_1+p_2=p_s$, $z_{s1}=-t_f\phi$, $z_{s2}=t_f\phi$, $z_{u1}=-t_f\phi_u$, and $z_{u2}=t_f\phi_u$, we can further rewrite Eq. (15) as

$$-4A_c t_f\frac{d}{dt}(\phi-\phi_u)+\frac{1}{\beta_e}(V_{10}+V_{20})\frac{d}{dt}(p_1-p_2)+(2C_{ip}+C_{ep})(p_1-p_2)=Q_1-Q_2. \tag{16}$$

For simplicity, we assume that the displacement of spool valve z_v is directly proportional to electric voltage $u_v(t)$, namely, $z_v=k_v u_v(t)$, where k_v is a known scalar.

The flow quantities in the two circuits can be presented as [38]

$$\begin{cases} Q_1 = k_u u_v(s(u_v)\sqrt{p_s-p_1}+s(-u_v)\sqrt{p_1-p_r}), \\ Q_2 = k_u u_v(s(-u_v)\sqrt{p_s-p_2}+s(u_v)\sqrt{p_2-p_r}), \end{cases} \tag{17}$$

where

$$k_u = k_v C_d w\sqrt{\frac{2}{\rho}},\ s(u_v)=\begin{cases}1, & u_v\geqslant 0,\\ 0, & u_v<0.\end{cases} \tag{18}$$

where C_d is the discharge coefficient, w is the spool valve area gradient, and p_r is the return pressure which equals to the atmospheric pressure generally.

4 Experiments and simulations

4.1 Model verification and numerical simulations

In this section, the proposed vehicle model is validated against experimental test results. A novel fully electric vehicle prototype is utilized to conduct various maneuvers, as shown in Fig. 3. The parameters of the vehicle model in the simulations, which will be illustrated in the next section, are identical to those of this vehicle, as listed in Table I in the Appendix. Table II shows the parameters of the servo-valve electro-hydraulic actuator.

Fig. 3 Fully electric vehicle on a concrete pavement in the experimental tests.

The experimental setup and corresponding devices are depicted in Fig. 4. A wheel torque meter is utilized to record the wheel steering angle with a steering ratio of 17.5. A velocity recorder, namely, RACELOGIC VBOX 3i, is used to obtain vehicle velocity v_x with the GPS navigation system. An inertial measurement unit (IMU) sensor is utilized to record yaw rate $\dot{\psi}$, roll angle ϕ, and lateral acceleration a_y. These signals are then transferred to a laptop for further signal post-processing.

The two different types of maneuver, namely, sine-wave and double lane change, are executed to validate the vehicle model by comparing the test and simulation results. The vehicle speeds are 40 and 80 km/h. The results are shown in Figs. 5 and 6.

Figure 5 shows the vehicle response comparisons at sine-wave maneuver. Considering that transient responses for the beginning and end of the sine-wave maneuver cannot be used to characterize vehicle performance, defining an effective time interval would be helpful. Here, the effective time interval starts at 3.9 s and ends at

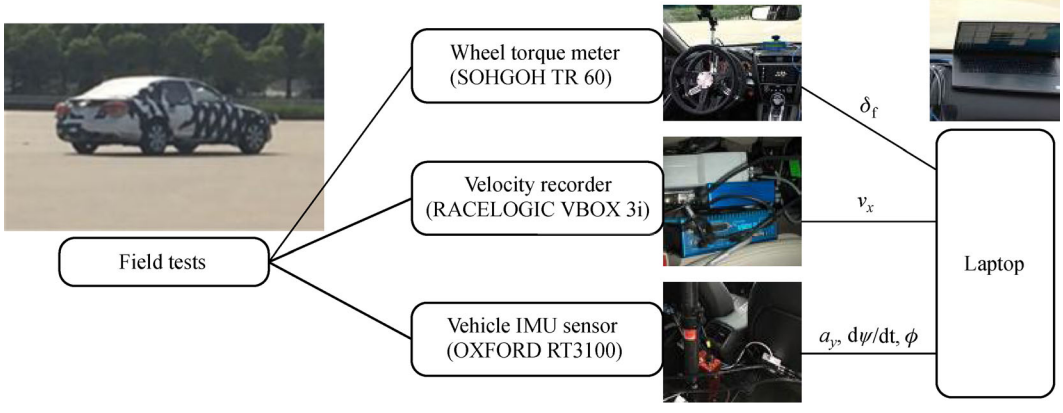

Fig. 4 Experimental setup.

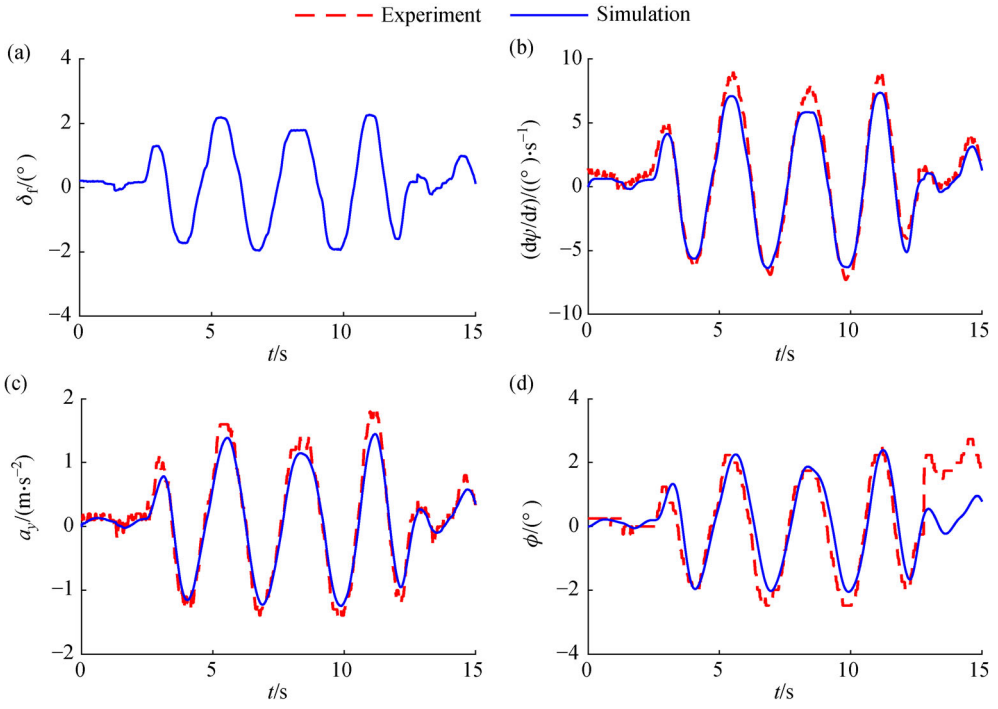

Fig. 5 Comparisons of simulation and experiment results at sine-wave maneuver: (a) Sine-wave steering angle, (b) yaw rate, (c) lateral acceleration, and (d) roll angle of sprung mass.

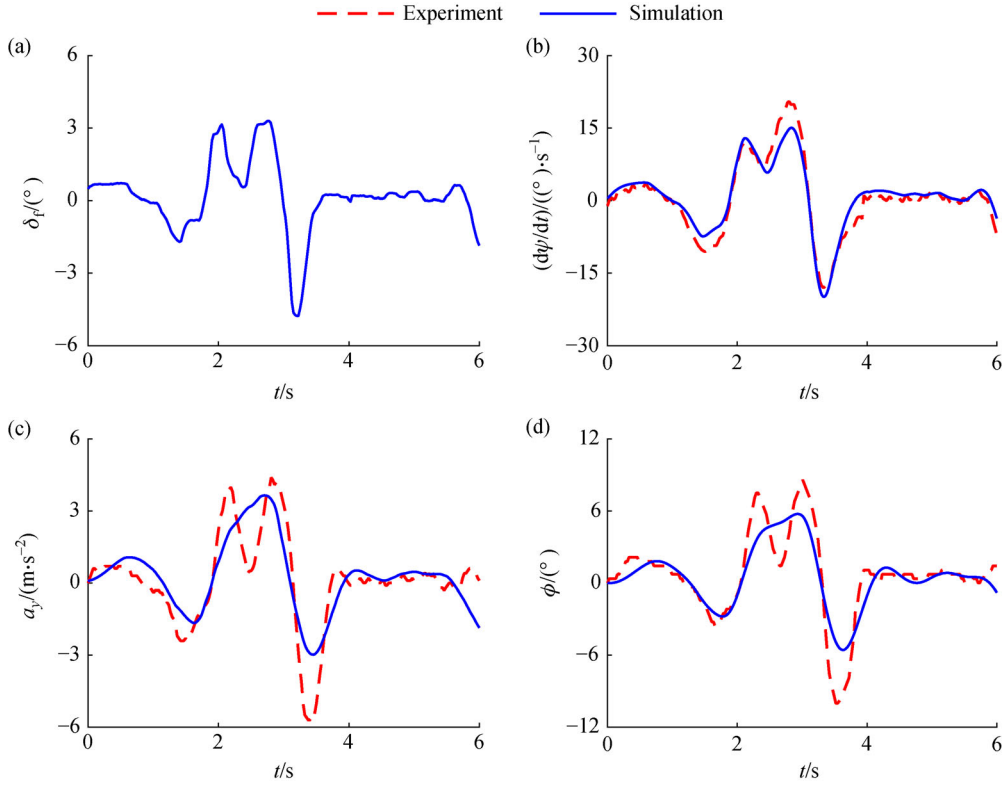

Fig. 6 Comparisons of simulation and experiment results at double-lane-change maneuver: (a) Sine-wave steering angle, (b) yaw rate, (c) lateral acceleration, and (d) roll angle of sprung mass.

11.1 s. Figure 5(a) shows the tire steering angle transferred from the steering wheel via the steering system that is utilized as the input of the subsequent simulations. Figure 5(b) shows that the yaw rate of the simulation fits that of the experimental result well, except that the peak values of the latter are smaller than the former. The reason for this result may be the filter embedded in the IMU sensor, which cuts off the signal peaks. Figure 5(c) shows that the lateral accelerations of the two signals are close to each other. Figure 5(d) indicates that the two roll angle responses fit well, but steady shift exists after the steering maneuver is finished.

Figure 6 presents the vehicle responses of double-lane-change maneuver, which is used to compare the aperiodic dynamic characteristics with those of the sine-wave maneuver. Figure 6(a) shows the tire steering input for the experiment and simulation. Figure 6(b) shows the yaw rates for the two maneuvers. The figure reveals that although discrepancies exist in the transient behaviors of the two maneuvers, the general response tendencies are the same. The discrepancies may be attributed to the tire transient properties and several chassis apparatuses, such as rubber bushes, which are not formulated in the proposed vehicle model due to their complicated dynamic characteristics and minor importance in vehicle responses compared with suspension devices. Figure 6(c) shows that the simulation and experiment results have almost the same lateral accelerations. Figure 6(d) reveals that the roll angles in the simulation and experiment fit well. Thus, we conclude that the simulation results match the experimental results well, thereby validating the proposed vehicle model.

4.2 Validation of the control scheme

Simulations are conducted under the two steering maneuvers to validate the proposed control scheme and investigate the effectiveness of the LQR controller with electro-hydraulic suspension. Vehicle responses, including suspension deflection z_{su} at the left-front station, roll angle ϕ, lateral load transfer rate (LTR) [39], and tire-terrain contact force F_{tz1} at the left-front station, are compared and analyzed. Meanwhile, the dynamic responses of the electro-hydraulic suspension, including roll-resistant moment $u(t)$, electric voltage $u_v(t)$, oil pressure p_i, and flow quantity Q_i at the two oil circuits, are also derived.

Figure 7 shows the vehicle dynamic responses under sine-wave maneuver for uncontrolled and controlled schemes. Figure 7(a) reveals that during the effective time interval, the suspension deflection is reduced by more than 30.7% with the RREHS subsystem. Figure 7(b) illustrates that the roll angle response is decreased by 29.2% or more with the proposed controller. Figure 7(c) indicates that LTR is decreased by over 10.7% during the effective time interval, which implies that vehicle roll stability is effectively enhanced. Figure 7(d) shows that tire force is reduced by 1.1% at the left-front station. Therefore, vehicle performance is improved by the electro-hydraulic suspension.

Figure 8 shows the dynamic responses of the electro-hydraulic suspension. Figure 8(a) indicates that a roll-resistant moment is imposed on the vehicle when the vehicle performs turning maneuver to enhance vehicle roll stability. Figure 8(b) shows the electric voltage required by the servo-valve to generate the desired roll-resistant moment. Figure 8(c) depicts the oil pressures of the two oil circuits in the RREHS subsystem, which can be derived with the desired moment $u(t)$ and suspension geometry. Figure 8(d) shows the fluid flow quantities at the two circuits.

The vehicle and servo-valve responses under double-lane-change maneuver are also investigated, as shown in Figs. 9 and 10. In Fig. 9(a), the suspension deflection is decreased by 24.1% at $t = 3.01$ s and by 46.7% at $t = 3.75$ s. Figure 9(b) shows that roll angle ϕ is decreased by more than 25.5% during the time interval [2.8, 4.0] s. In Fig. 9(c), we can observe that the LTR value is reduced by 28.9% at $t = 3.68$ s, whereas it is only reduced by 0.6% at $t = 2.97$ s. Figure 9(d) shows that the maximum tire force is slightly decreased.

Roll-resistant moment $u(t)$ is derived in Fig. 10(a). The corresponding electric voltage $u_v(t)$ required by the servo-valve is shown in Fig. 10(b). Figure 10(c) shows the obtained fluid pressures at the two fluid circuits of the RREHS subsystem. Figure 10(d) displays the fluid quantities Q_i at the two circuits.

5 Conclusions

This study proposes a roll-resistant electro-hydraulic suspension to enhance vehicle roll stability when a vehicle is performing steering maneuvers. A 4-DOF vehicle model is proposed to investigate the integration of lateral and roll dynamics. Then, an RREHS subsystem is developed to enhance vehicle roll motion, and an LQR optimal control scheme is used to derive the roll-resistant moment. In addition, the vehicle model is validated against field experiment results. The effectiveness of the optimal control scheme is verified by implementing the scheme on the RREHS subsystem. The following conclusions are derived from the results. (1) A 4-DOF vehicle model that incorporates yaw and roll motions is derived and validated. (2) The optimal controlled RREHS subsystem can be utilized to enhance vehicle performance effectively, especially roll stability, under sine-wave and double-lane-change steering maneuvers.

Considering the differences in theoretical equations, numerical models, and engineering applications, validation of the equation through experiments is recommended. In our future work, the proposed controller will be experimented on by using a real vehicle.

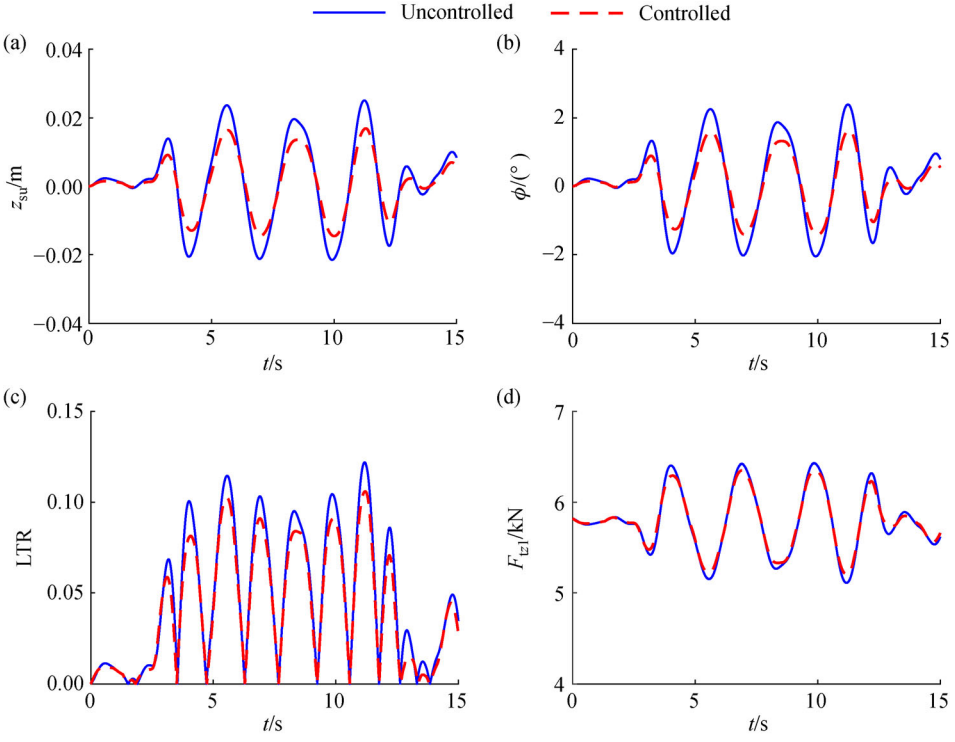

Fig. 7 Vehicle responses under sine-wave steering maneuver at 40 km/h: (a) Suspension deflection z_{su} at the left-front station, (b) roll angle ϕ; (c) lateral load transfer rate, and (d) tire-terrain contact force F_{tz1}.

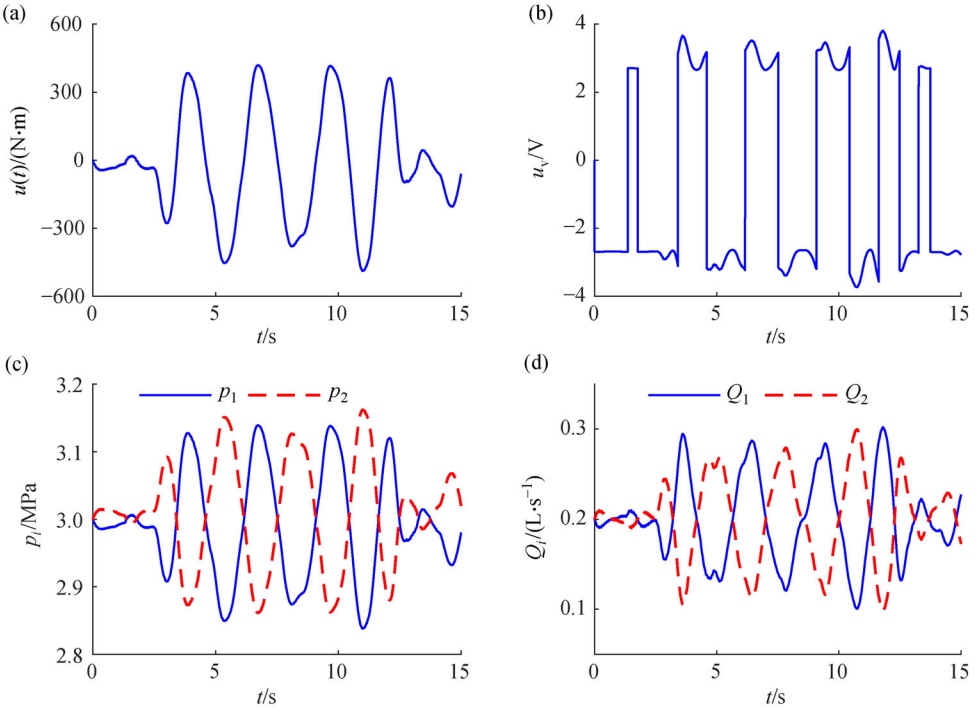

Fig. 8 Dynamic responses of the electro-hydraulic suspension under sine-wave maneuver: (a) Roll-resistant moment $u(t)$, (b) electric voltage of the servo-valve, (c) oil pressures at the two hydraulic circuits, and (d) flow quantities at the two circuits.

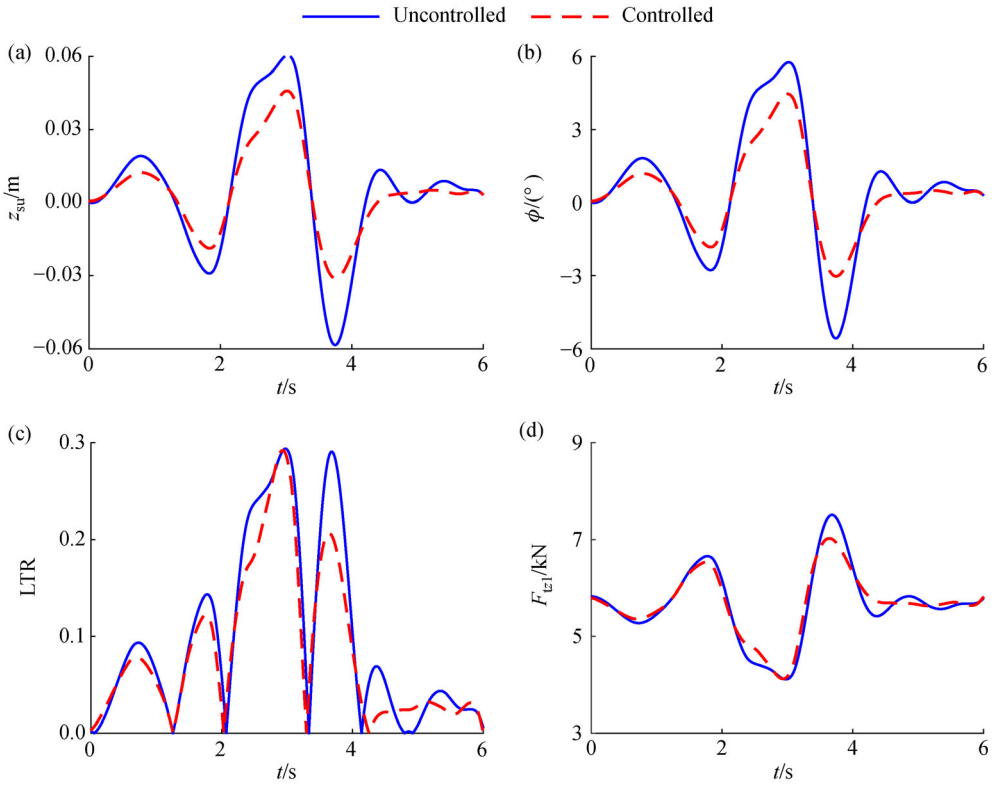

Fig. 9 Vehicle responses under double-lane-change steering maneuver at 80 km/h: (a) Suspension deflection z_{su} at the left-front station, (b) roll angle ϕ; (c) lateral load transfer rate, and (d) tire-terrain contact force F_{tz1}.

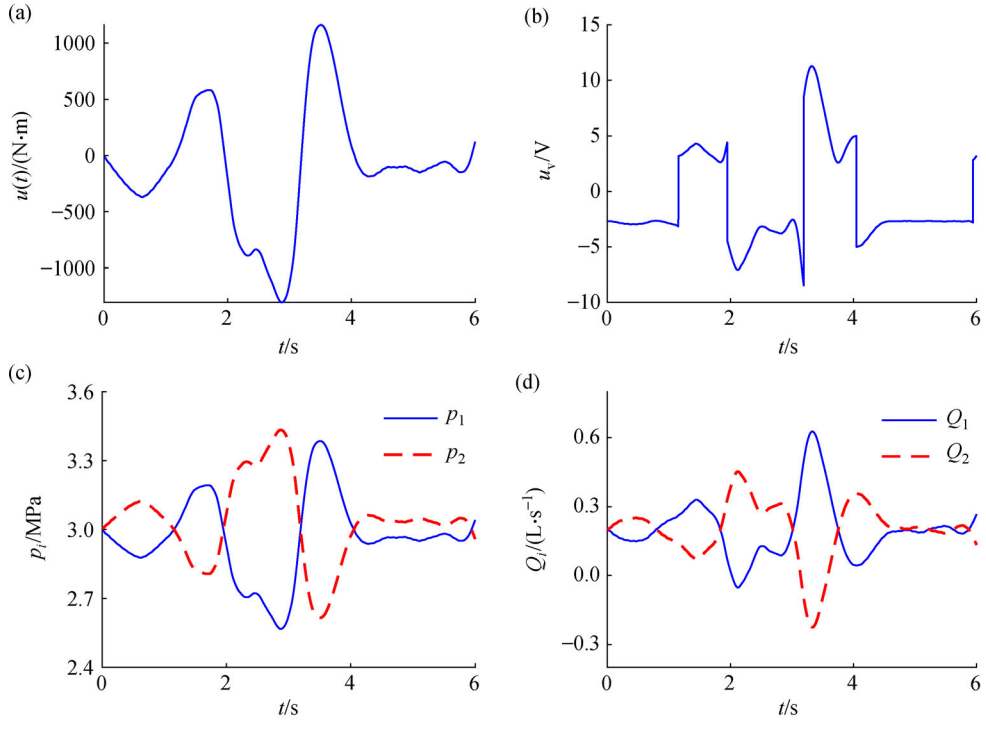

Fig. 10 Dynamic responses of the electro-hydraulic suspension under double-lane-change steering maneuver: (a) Roll resistant moment $u(t)$, (b) electric voltage of the servo-valve, (c) oil pressures at the two hydraulic circuits, and (d) flow quantities at the two circuits.

Appendix

Table I Vehicle parameters

Variable	Value	Description
m_s/kg	1934	Sprung mass
I_s/(kg·m^2)	560	Roll inertia of sprung mass
I_{zz}/(kg·m^2)	1640	Yaw inertia of the vehicle
I_{uyy}/(kg·m^2)	10	Rotation inertia of the tire
m_{uf}/kg	63	Unsprung mass in the front axle
m_{ur}/kg	57	Unsprung mass in the rear axle
c_{sf}/(N·s·m^{-1})	2000	Damping coefficient of front suspension
c_{sr}/(N·s·m^{-1})	2200	Damping coefficient of rear suspension
c_{tf}/(N·s·m^{-1})	100	Damping coefficient of the front tire
c_{tr}/(N·s·m^{-1})	100	Damping coefficient of the rear tire
k_{sf}/(N·m^{-1})	36800	Spring stiffness of front suspension
k_{sr}/(N·m^{-1})	33800	Spring stiffness of rear suspension
k_{tf}/(N·m^{-1})	278000	Front tire vertical stiffness
k_{tr}/(N·m^{-1})	265000	Rear tire vertical stiffness
l_f/m	1.33	Length from CG to the front axle
l_r/m	1.62	Length from CG to the rear axle
t_f/m	0.81	Half-track width in the front axle
t_r/m	0.81	Half-track width in the rear axle
h_{os}/m	0.43	Height from vehicle rolling center to CG of sprung mass
h_{oc}/m	0.11	Height from vehicle rolling center to chassis bottom
i_{sw}	17.5	Steering ratio

Table II Parameters of the servo-valve electro-hydraulic actuator [33]

Variable	Value	Description
A_h/m^2	0.0013	Section area of the hydraulic cylinders
V_0/m^3	3.77×10^{-4}	$V_0 = V_{10} + V_{20}$; total oil volume in each cylinder
p_s/MPa	6.0	Supply pressure
k_x/(m^2·s)	2.5	Valve flow gain coefficient
k_p/(m^5·N^{-1}·s^{-1})	4.2×10^{-11}	Total flow pressure coefficient
C_{tp}	0	$C_{tp} = 2C_{ip} + C_{ep}$; total leakage coefficient of the RREHS subsystem
β_e/(N·m^{-2})	6.89×10^6	Effective bulk modulus of the oil
k_v/(m·A^{-1})	0.0239	Servo-valve gain

Acknowledgements This work was supported by the National Natural Science Foundation of China (Grant No. 5187051675) and the Natural Science Foundation of Hunan Province (Grant No. 2017JJ2031).

References

1. Boada B L, Boada M J L, Vargas-Melendez L, et al. A robust observer based on H_∞ filtering with parameter uncertainties

combined with neural networks for estimation of vehicle roll angle. Mechanical Systems and Signal Processing, 2018, 99: 611–623
2. Dahmani H, Pages O, El Hajjaji A, et al. Observer-based robust control of vehicle dynamics for rollover mitigation in critical situations. IEEE Transactions on Intelligent Transportation Systems, 2014, 15(1): 274–284
3. Yoon J, Cho W, Kang J, et al. Design and evaluation of a unified chassis control system for rollover prevention and vehicle stability improvement on a virtual test track. Control Engineering Practice, 2010, 18(6): 585–597
4. Rajamani R, Piyabongkarn D. New paradigms for the integration of yaw stability and rollover prevention functions in vehicle stability control. IEEE Transactions on Intelligent Transportation Systems, 2013, 14(1): 249–261
5. Lua C, Castillo-Toledo B, Cespi R, et al. Nonlinear observer-based active control of ground vehicles with non negligible roll dynamics. International Journal of Control, Automation, and Systems, 2016, 14(3): 743–752
6. Jin Z, Zhang L, Zhang J, et al. Stability and optimised H_∞ control of tripped and untripped vehicle rollover. Vehicle System Dynamics, 2016, 54(10): 1405–1427
7. Yang Y, Ren W, Chen L, et al. Study on ride comfort of tractor with tandem suspension based on multi-body system dynamics. Applied Mathematical Modelling, 2009, 33(1): 11–33
8. Sancibrian R, Garcia P, Viadero F, et al. Kinematic design of double-wishbone suspension systems using a multiobjective optimisation approach. Vehicle System Dynamics, 2010, 48(7): 793–813
9. Mahmoodi-Kaleibar M, Javanshir I, Asadi K, et al. Optimization of suspension system of off-road vehicle for vehicle performance improvement. Journal of Central South University of Technology, 2013, 20(4): 902–910
10. Pang H, Liu F, Liu X. Enhanced variable-universe fuzzy control for vehicle semi-active suspension systems. Journal of Intelligent & Fuzzy Systems, 2016, 31(6): 2999–3006
11. Cheng M X, Jiao X H. Observer-based adaptive L_2 disturbance attenuation control of semi-active suspension with MR damper. Asian Journal of Control, 2017, 19(1): 346–355
12. Tang X, Du H, Sun S, et al. Takagi-Sugeno fuzzy control for semi-active vehicle suspension with a magnetorheological damper and experimental validation. IEEE/ASME Transactions on Mechatronics, 2017, 22(1): 291–300
13. Gáspár P, Szabó Z, Szederkényi G, et al. Design of a two-level controller for an active suspension system. Asian Journal of Control, 2012, 14(3): 664–678
14. Li H, Liu H, Hilton C, et al. Non-fragile H_∞ control for half-vehicle active suspension systems with actuator uncertainties. Journal of Vibration and Control, 2013, 19(4): 560–575
15. Bououden S, Chadli M, Karimi H R. A robust predictive control design for nonlinear active suspension systems. Asian Journal of Control, 2016, 18(1): 122–132
16. Wang G, Chen C, Yu S. Optimization and static output-feedback control for half-car active suspensions with constrained information. Journal of Sound and Vibration, 2016, 378: 1–13
17. Oustaloup A, Moreau X, Nouillant M. The CRONE suspension. Control Engineering Practice, 1996, 4(8): 1101–1108
18. Quaglia G, Sorli M. Air suspension dimensionless analysis and design procedure. Vehicle System Dynamics, 2001, 35(6): 443–475
19. Ahmadian M, Simon D E. An analytical and experimental evaluation of magneto rheological suspensions for heavy trucks. Vehicle System Dynamics, 2002, 37(sup1): 38–49
20. Kang J, Yoo J, Yi K. Driving control algorithm for maneuverability, lateral stability, and rollover prevention of 4WD electric vehicles with independently driven front and rear wheels. IEEE Transactions on Vehicular Technology, 2011, 60(7): 2987–3001
21. Du H, Zhang N. Fuzzy control for nonlinear uncertain electro-hydraulic active suspensions with input constraint. IEEE Transactions on Fuzzy Systems, 2009, 17(2): 343–356
22. Choi H D, Lee C J, Lim M T. Fuzzy preview control for half-vehicle electro-hydraulic suspension system. International Journal of Control, Automation, and Systems, 2018, 16(5): 2489–2500
23. Sun W, Gao H, Yao B. Adaptive robust vibration control of full-car active suspensions with electrohydraulic actuators. IEEE Transactions on Control Systems Technology, 2013, 21(6): 2417–2422
24. Kim H J. Robust roll motion control of a vehicle using integrated control strategy. Control Engineering Practice, 2011, 19(8): 820–827
25. Yim S. Design of a preview controller for vehicle rollover prevention. IEEE Transactions on Vehicular Technology, 2011, 60(9): 4217–4226
26. Huang H H, Yedavalli R K, Guenther D A. Active roll control for rollover prevention of heavy articulated vehicles with multiple-rollover-index minimization. Vehicle System Dynamics, 2012, 50(3): 471–493
27. Imine H, Fridman L M, Madani T. Steering control for rollover avoidance of heavy vehicles. IEEE Transactions on Vehicular Technology, 2012, 61(8): 3499–3509
28. Dal Poggetto V F, Serpa A L. Vehicle rollover avoidance by application of gain-scheduled LQR controllers using state observers. Vehicle System Dynamics, 2016, 54(2): 191–209
29. Sun H, Chen Y H, Zhao H. Adaptive robust control methodology for active roll control system with uncertainty. Nonlinear Dynamics, 2018, 92(2): 359–371
30. Pourasad Y, Mahmoodi-K M, Oveisi M. Design of an optimal active stabilizer mechanism for enhancing vehicle rolling resistance. Journal of Central South University, 2016, 23(5): 1142–1151
31. Marzbanrad J, Soleimani G, Mahmoodi-K M, et al. Development of fuzzy anti-roll bar controller for improving vehicle stability. Journal of Vibroengineering, 2015, 17(7): 3856–3864
32. Kawamoto Y, Suda Y, Inoue H, et al. Electro-mechanical suspension system considering energy consumption and vehicle manoeuvre. Vehicle System Dynamics, 2008, 46(sup1): 1053–1063
33. Yim S, Jeon K, Yi K. An investigation into vehicle rollover prevention by coordinated control of active anti-roll bar and electronic stability program. International Journal of Control, Automation, and Systems, 2012, 10(2): 275–287
34. Wang L, Todaria P, Pandey A, et al. An electromagnetic speed bump energy harvester and its interactions with vehicles. IEEE/ASME Transactions on Mechatronics, 2016, 21(4): 1985–1994
35. Jin X, Yin G. Estimation of lateral tire-road forces and sideslip angle for electric vehicles using interacting multiple model filter approach.

Journal of the Franklin Institute-Engineering and Applied Mathematics, 2015, 352(2): 686–707

36. Mashadi B, Mahmoodi-K M, Kakaee A H, et al. Vehicle path following control in the presence of driver inputs. Proceedings of the Institution of Mechanical Engineers, Part K: Journal of Multi-body Dynamics, 2013, 227(2): 115–132
37. Vu V T, Sename O, Dugard L, et al. Enhancing roll stability of heavy vehicle by LQR active anti-roll bar control using electronic servo-valve hydraulic actuators. Vehicle System Dynamics, 2017, 55(9): 1405–1429
38. Ding W, Deng H, Xia Y, et al. Tracking control of electro-hydraulic servo multi-closed-chain mechanisms with the use of an approximate nonlinear internal model. Control Engineering Practice, 2017, 58: 225–241
39. Rath J J, Defoort M, Veluvolu K C. Rollover index estimation in the presence of sensor faults, unknown inputs, and uncertainties. IEEE Transactions on Intelligent Transportation Systems, 2016, 17(10): 2949–2959